A Wearable CMOS Impedance to Frequency Sensing System for Non-Invasive Impedance Measurements

Ava Hedayatipour, Member, IEEE, Shaghayegh Aslanzadeh, Member, IEEE,
Shahram Hatefi Hesari, Graduate Student Member, IEEE,
Mohammad Aminul Haque, Graduate Student Member, IEEE, and Nicole McFarlane, Senior Member, IEEE

Abstract—In this paper, we demonstrate a novel non-invasive, wearable impedance sensor. The impedance sensor, using an impedance to frequency measurement, with two modes of resistance and capacitance measurement is implemented in CMOS 130 nm technology. The sensor consisting of current and voltage comparators for different mode of measurement, has a low power consumption of 30 μW per channel. The sensor is demonstrated in two applications, thoracic impedance and hand gesture recognition. Thoracic impedance is based on impedance modulation through fluid accumulation. Hand gestures are detected through tissue impedance sensing. The full thoracic impedance sensing system is smaller than a credit card, low cost, and consumes 3 mW which includes the sensor, transmitter, and power control unit. Data received by this sensor can be easily transferred for further processing and, eventually, detection of heart failure. The electrodes were implemented using conductive paint, and the system was validated using passive loads to represent human tissue models and test subjects. The hand gesture system operates on 600 μW with the maximum number of electrodes, and uses adhesive copper with electrical paint as electrodes.

Index Terms—Bioimpedance, flexible electronics, hand gesture recognition, heart failure, impedance measurement, wearable sensors.

I. INTRODUCTION

LECTRICAL impedance measurement of biological tissues have been studied for many different biomedical applications. In this measurement, an electric field between two electrodes is modulated by the position, and density of tissue (or particles) between the electrodes. This modulated electric field can be measured as a current change. Bio-impedance measurements can be performed without resorting to invasive procedures and has thus been considered as a promising technology for clinical monitoring for body composition [1], [2], respiration analysis and cardiac output estimation [3]–[5], cardiac monitoring [6]–[9], obesity management [10], and tracking body

Manuscript received June 9, 2020; revised August 6, 2020 and September 4, 2020; accepted September 11, 2020. Date of publication September 18, 2020; date of current version October 15, 2020. This work was supported by the National Science Foundation under Grant 1816703. This article was recommended by Associate Editor Dr. Leanne Lai Hang Chan. (Corresponding author: Ava Hedavatipour.)

The authors are with the Department of Electrical Engineering and Computer Science, University of Tennessee, Knoxville, TN 37996 USA (e-mail: ahedaya1 @vols.utk.edu; saslanza@vols.utk.edu; hesari@vols.utk.edu; mhaque4@vols.utk.edu; mcf@utk.edu).

Color versions of one or more of the figures in this article are available online at https://ieeexplore.ieee.org.

Digital Object Identifier 10.1109/TBCAS.2020.3025218

fluid shifts during physical activity [11]. There have been many studies regarding impedance sensing to improve heart failure outcomes. Two of the most trialed applications are intra-thoracic and trans-thoracic electrical impedance [12]. Gesture recognition is among other promising applications, practical for medical needs or next generation smart watches [13]. With the increase of continuous monitoring applications, portable or even wearable systems are desirable. Even microcontroller based impedance measurement systems [14]–[16] are becoming obsolete in favor of integrated sensing systems because of area and power consumption [17]. We demonstrate our impedance sensing system using two applications, heart failure and gesture recognition.

Heart failure causes insufficient blood flow to organs with normal pressure. Acute decompensated heart failure, (ADHF), results from deteriorating heart function and is a frequent cause of recurrent hospital admissions. Identification of those at risk for rehospitalization is of prime importance. Many methods monitor symptoms that appear late. This increases the chance that the subject is sent to the ICU which can be costly. Self-care for chronic heart failure can be done by measuring intra-thoracic impedance as a sign of fluid accumulations in the thorax [18]–[20]. Repetitive hospitalizations in heart failure patients can be reduced by setting alarms based solely on intra-thoracic impedance or combination of weight, ECG, and impedance [19], [21], [22].

However, not all heart failure patients are candidates for implantable devices due to invasiveness and cost. Therefore, flexible, wearable trans-thoracic electrical impedance measurement systems to prevent heart failure are being studied [24]–[28]. These electrodes can be implemented in patches and textile. In [25], a 15 cm \times 15 cm patch sensor is proposed that monitors thoracic impedance and ECG with low-power and high resolution in a wearable low cost cardiac healthcare system. Textile electrode implementation has a dry interface between the skin and the electrode resulting in an increased impedance in series with the current injecting electrodes [26]. The design proposed in [28] has electrodes to measure thoracic impedance implemented in a T-shirt. Using stretchy textile material for improved contact has also been used [27], however, these materials may be less comfortable for elderly patients. For better contact, wet textile electrodes could improve charge transfer between the electrode and skin and facilitate better textile-based impedance measurement [29]. Using up to 32 electrodes around the chest in [30], system implementation for electrical impedance

1932-4545 © 2020 IEEE. Personal use is permitted, but republication/redistribution requires IEEE permission. See https://www.ieee.org/publications/rights/index.html for more information.

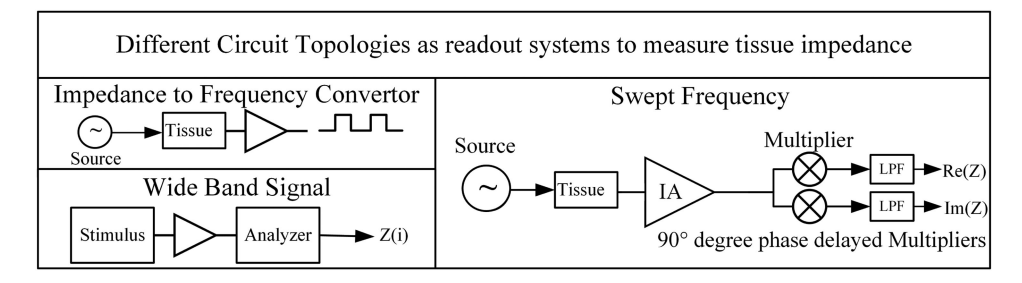


Fig. 1. Different topologies as readout system for impedance measurement.

tomography with a single-ended phasic voltage was presented. Using heavy computational requirements, accurate measurement is derived from of an image of thoracic tissues. We propose a 10 g trans-thoracic impedance measurement system that is adhered to the chest using medical tape and facilitates low impedance connection to skin with conductive electrical paint.

In our second demonstrated application, non-invasive, high accuracy recognition of hand gestures is realized through impedance measurements. This system can be incorporated in the next generation of smartwatches to be used in real-time translation of sign language or as an interactive interface with smart devices. Before the use of wearable sensors, hand gesture recognition was implemented using cameras where a picture is taken for a single gesture and sent out for classification [31]. However, an imaging system requires a line of sight, has a heavy computational load, and uses expensive equipment. Thus, there is a need for cheaper, portable devices. In [32], [33] discrete hand gestures are recovered using the interior impedance geometry of a user's arm. This application, called Tomo (impedance measurement for tomography), is one of the few systems that uses a wearable system to recognize hand gestures.

Among portable hand gesture recognition designs, there are other sensors modules which are utilized [34]–[36]. In [34], Jung et al. uses air pressure sensors, which are large in size, allowing only few sensors around the wrist. In [35], a polymeric strain gauge sensor is used to identify movements employed for rehabilitation and [36] uses flexible capacitive pressure. These two sensors lack accuracy and recognise only a few patterns. In a more recent design, FPGA implemented a neural network along with commercial ICs were used for a high-performance hand gesture recognition [37], [38]. In [38], a human-machine interface operates as a link between the user and a hand prosthesis using an array of electrodes on the user's forearm to create a bio-impedance image. [39] presented a partial integration of a 16-electrode electrical impedance tomography system, implemented in CMOS where an FPGA is used for impedance extraction and the excitation signal is provided by a fabricated current-steering DAC. To reduce computational load, power consumption, device area, and increase accuracy, we use an integrated impedance sensor. This sensor facilitates having more that 32 arrays around the wrist.

This paper presents a wearable CMOS impedance to frequency converter suitable for our two applications of choice, non-invasive measurements of thoracic impedance and hand gesture recognition. Preliminary results of the impedance

measurement circuit only was presented in [40]. Here we expand to include the sine wave generator, electrodes, and wireless transmission into a wearable sensor. To the best of our knowledge this is the first time a low power implementation of analog CMOS devices has been used for these applications. The low power implementation and small size of these circuits will lead to increased battery life for wearable devices and increased accuracy.

Among impedance measurement topologies available (Fig. 1) [41], conversion to frequency or using lock-in amplifier to extract the real and imaginary part of impedance [23], [42]–[49] are more suitable for wearable systems. The frequency conversion topology is less power consuming. To the best of our knowledge, our topology is the first correlating current change to resistance and delay to measure capacitance with only 4 circuit blocks. The output of our system is frequency, which can be transmitted without the need for bulky and power-consuming analog to digital converters. Using a custom impedance measurement circuit makes this system have the lowest weight and power consumption among the state of art designs. The whole system can be attached to the skin using medical tape and does not need tight clothing or uncomfortable straps. The design and implementation of the impedance measurement system and sine wave generator is discussed in section II. Simulation and experimental results for the system and its application in hand gesture and transthoracic impedance measurements are discussed in section III. Finally section IV gives the conclusion.

II. DESIGN STRATEGY AND SPECIFICATIONS

The overall design is shown in Fig. 2(a). The input is an alternating AC voltage that goes through the tissue. The voltage and the frequency cannot be sensed by humans. Comparators then operate in 2 phases which measures the electrode potential and current. In the resistance sensing phase, the current is compared to a reference current, the amplitude is therefore proportional to the resistance. The current is,

$$i = \frac{V_{\text{ref}}\sin(\omega t)}{Z_R} \tag{1}$$

where i is the current through the cell, $v_{\rm ref}$ is the amplitude of the excitation signal, ω is the frequency, and Z_R is the cell's resistance.

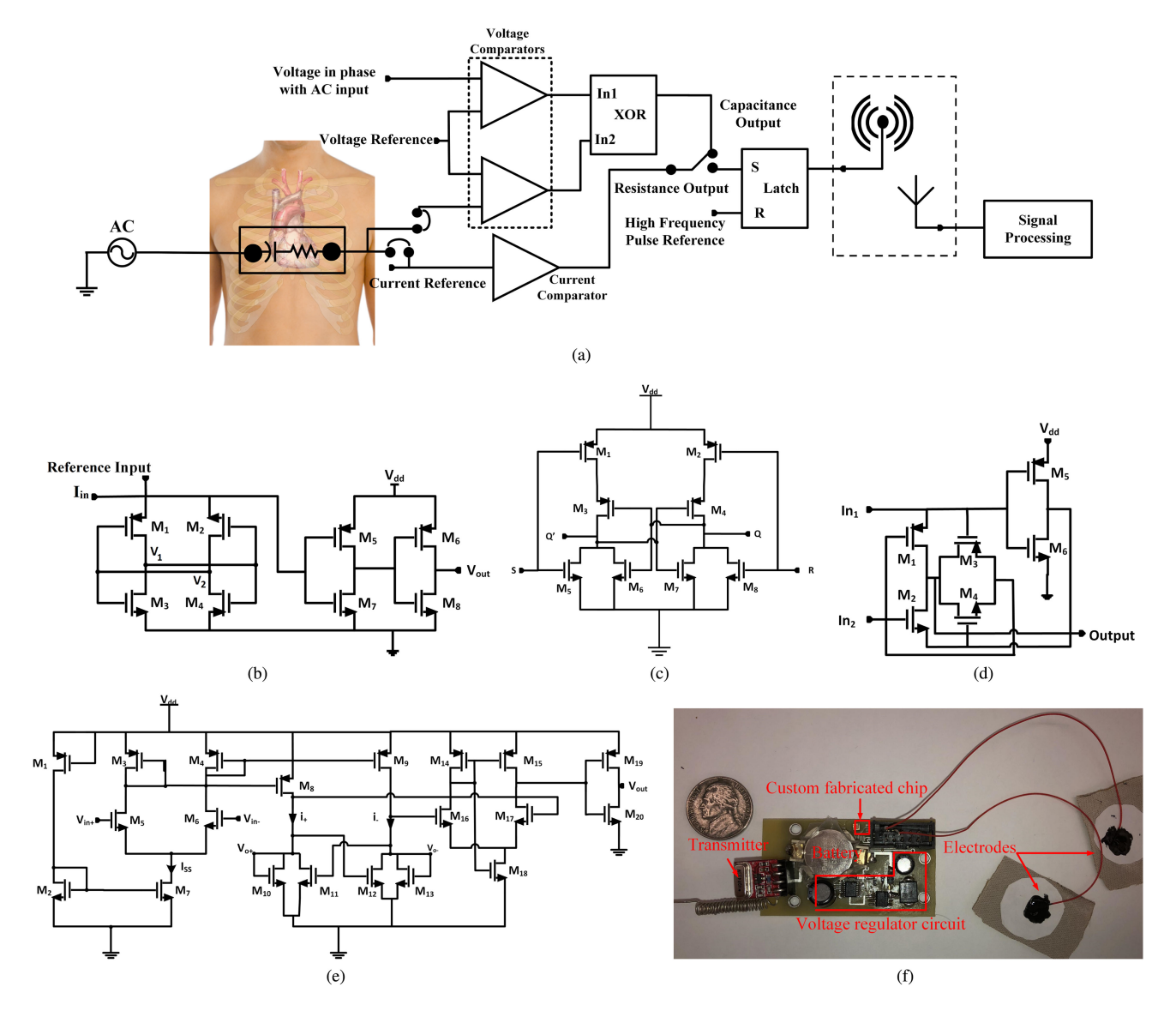


Fig. 2. (a) Proposed impedance to frequency design (human body picture taken from [50]) that includes (b) a low power current comparator to measure resistance, (c) SR-latch circuit, to convert pulse width resulting from the measured resistance to a high frequency pulse train, (d) XOR gate circuit to detect the phase change between a reference signal and signal processing through a tissue, and (e) voltage comparator circuit to detect the difference of a constant voltage crossing between a reference signal and signal passing through tissue. (f) The thoracic impedance measurement system.

Using a comparator that switches between low and high, the changes in current is monitored. An increase in input voltage results in an increase in the input current. When the current increases above the reference voltage, the output of the current comparator goes high. This happens since the difference between the reference current (I_0) and the measured current is positive, thus, $I_0 - \frac{V_{\rm ref} Sin(\omega t)}{Z_R} > 0$. As the current falls back below the reference current the voltage goes low. Since the input frequency is fixed, the period of the output stays the same with changing of input impedance. However, the pulse width is dependent on the input resistance. The pulse width of the high signal is,

$$PW_R = \left(\sin^{-1}\frac{I_0 Z_R}{V_{\text{ref}}}\right)/\omega \tag{2}$$

where PW_R is the pulse width associated with the resistance.

For both resistance and capacitance measurement, the references are created by a potentiometer and supply voltage. In future designs, these references will be replaced by dynamic circuits.

For capacitance measurement, voltage comparators detect a constant voltage crossing. Because of the change in phase, the signal going through a tissue crosses zero (or any other constant voltage) at a different time, than the reference AC stimulating signal. The difference in time for the original and delayed signal phase (ϕ) crossing a voltage is detected by the XOR,

$$PW_c = \phi = \tan^{-1} \left(\frac{j\Delta Z_C \omega}{R} \right) \tag{3}$$

where PW_C is the pulse width, associated with the phase difference detected by our XOR, ΔC is the change in capacitance,

and j is $\sqrt{-1}$. Both modules give information in terms of pulse width.

Pulse width is not a convenient parameter to be measured by other analog blocks or to be translated to digital values to be saved in memories. Thus, we use an SR-latch as a high frequency modulator to translate the pulse width to a high frequency pulse train. An input pulse that can be generated using a VCO and that has a higher frequency, is connected to the reset pin of the SR-latch. This makes the pulses have a higher frequency as long as the output of the current comparator is high. When the output of the current comparator drops to ground, the output of the latch stays low. Using this method, with a larger pulse width, a higher frequency pulse train is seen at the output of the SR-latch. Assuming the PW_C or PW_R have the pulse width n times the pulse width of SRlatch, the R and C can hence be associated with the number of pulses n_{pulse} . To calculate n_{pulse} , the number of pulses in a given time period, the resistance measurement can be written using its Fourier series representation,

$$x_R(t) = \sum_{-\infty}^{\infty} \frac{1}{i\pi n} e^{\frac{j2\pi nt}{T_R}} \tag{4}$$

Assuming a pulse width T_{ref} , the reference signal is,

$$x_{reference}(t) = \sum_{-\infty}^{\infty} \frac{1}{i\pi n} e^{\frac{j2\pi nt}{T_{\text{ref}}}}$$
 (5)

The number of smaller reference pulses that can fit into the larger resistance measurement is the ratio of the reference and the measured resistance. This is given by,

$$n_{pulse} = \frac{\sum_{-\infty}^{\infty} e^{\frac{j2\pi nt}{T_R}}}{\sum_{-\infty}^{\infty} e^{\frac{j2\pi nkt}{T_{\text{ref}}}}}$$
 (6)

The sensor system operates from 100 Hz up to 1 MHz, this range is limited by the frequency of the transmitter used and the application the system is utilized for. This means that the system can be used with a large range of impedances by adjusting the stimulating signal. For tissue impedances based on values reported in [42], and other literature listed in comparison table in the conclusion, the frequency of 1–5 kHz was chosen as the stimulating signal in a single frequency mode. For hand gesture recognition, a frequency of 40 kHz is used. There have been studies comparing the use of single frequency versus swept frequency excitation for impedance measurement. Biological tissue is comprised of varying types of cells with a complex interconnected system consisting of water and other molecules and ions. Thus, higher frequencies versus lower frequencies in a multi-frequency based system can provide additional information about cells and tissues that only using a single frequency cannot. On the other hand, single-frequency devices are more economical, simpler to implement, and easier to use [51]. Given the chosen application, we take advantage of the simplicity of single frequency implementation. Here the input voltage of the VCO can be tuned manually to change the frequency. In addition, the excitation frequency used differs depending on the density of the tissue being measured. For the current resistance resolution the amplitude of the signal is chosen at 0.5 V peak-to-peak, contributing to current of 100 μ A-500 μ A using the limiting

resistors. Reducing the amplitude is proportional linearly with the reduction of resolution of the resistance measurement block.

It is worth mentioning that the same scheme of capacitive measurement can be used for inductive measurement. Here the delay caused by capacitor is measured, in case of an inductive load the signal lag would be measured. The XOR gate, however, has no means to detect if signal is leading or lagging. This could be implemented using a circuit that calculates the tangent of the load and differentiates between the inductor and capacitor by the sign of this component. In our design, since the tissue is modeled mostly as a capacitance, we only considered capacitive measurements. In the next section, the details for designing different blocks of our circuit are explained.

A. Sinusoidal Wave Generator

The first module in biomedical and chemical sensor microsystems is the compact signal generators. There are significant researches that solely work on tunable accurate sine wave generator implemented in CMOS technology. In [52], a signal generator was designed which produced analog sine waves from 4.8 Hz to 39 kHz with 330 μW of power. The signal generator was controlled by digital signals, which results in having better frequency accuracy, unlike the oscillators and nonlinear transform generators. [53] presented a low THD, low area, and low power sinusoidal current stimulator circuit for bio-impedance measurement. The design consisted of a recursive digital oscillator in order to generate the sine wave and embedded FIR filters combined with delta-sigma modulated 1 bit current source for digital-to-current conversion with a high resolution. The system consumed 55.6 μW for 20 kHz frequency. To characterize the base impedance measurement circuit without any possible errors from a signal generation circuit, functionality was initially performed with a benchtop function generator which is assumed to be ideal.

However, to have a complete portable system and determine the effects of the errors of a non-ideal sine wave generator, the sine wave generator was implemented using two methods, first using discrete components and second using an integrated onchip version. For the discrete sinusoidal wave generator an XR-2206 is used that does not need any programming to generate the wave and has a tunable frequency by changing the resistors and capacitors (Fig. 3). These discrete chips are becoming obsolete in favor of microcontroller-based sine wave generators. However, in our application, we targeted a low-power and low area design that pushed us to eliminate microcontrollers and use the XR-2206 instead. This discrete sine wave generator has symmetry adjusting and distortion tuning using two potentiometers. The system has the drawback of needing a separate power supply from our board (minimum 6.6 V) and high power consumption compared to other modules of our system (80 mW).

For the integrated circuit implementation, a standard current starved 5 stage VCO topology and a buffer, implemented in 180 nm CMOS technology, followed by an RC filter was used. The current starved VCO, operates over the frequency range of 100 Hz to 2.5 MHz, where a 0.1 V change results in 500 Hz change with wide dynamic range and linearity at significant

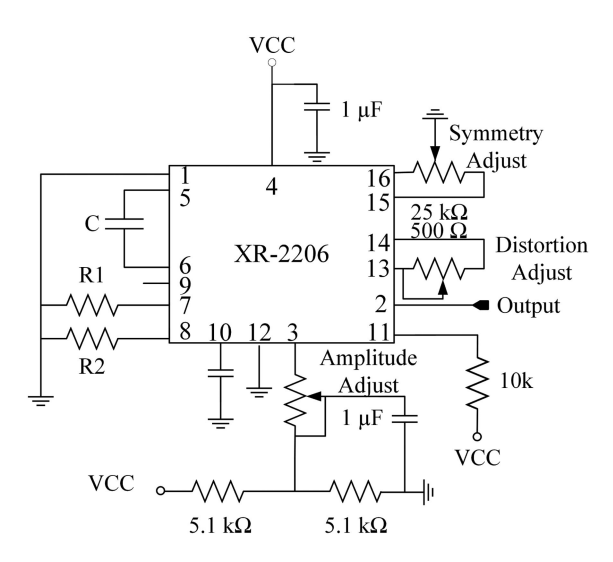


Fig. 3. XR2206 discrete chip to generate a sine wave [54].

low power. The transistor sizes were as follows, MP1, MP3 $= 6 \mu m/2\mu m$; MP2=60 $\mu m/2\mu m$; MN1, M5 = 3 $\mu m/2\mu m$; $MN2 = 40 \mu m/5 \mu m$; $MN3 = 3 \mu m/1 \mu m$; $MN4 = 30 \mu m/1 \mu m$. The digital buffer used 2 inverters where the first inverter has PMOS, NMOS aspect ratio of 6 μ m/2 μ m and 4 μ m/5 μ m respectively and the second inverter has PMOS and NMOS aspect ratio of 24 μ m/2 μ m and 16 μ m/5 μ m respectively. The output of this stage is a square wave, and a simple RC filter extracts the first harmonic of the square wave. The RC filter operates over a frequency range of a few kHz with a single R and C value. R and C need to be changed if the frequency changes more than a few kHz. However, this design is suitable for our application that stimulates the tissue at a single frequency. To mitigate any loading effects from the system another buffer was included using a MCP6004 discrete chip. This low power op-amp operates with voltage as low as 1.8 volt and sub-mW power consumption.

B. Current Comparator

The current-mode comparator determines if the received input signal (in the form of a current) exceeds a reference or pre-defined threshold current, and produces a voltage based on this comparison. Generally, current comparators are used in high-speed applications such as non-linear current-mode signal processing and analog to digital conversion. High resolution is another feature of current comparators which can be useful in current-mode image compression chips [55]. The design is illustrated in Fig. 2(b). As seen in this figure, both the changing and reference current go to one node. The design based on [56] in 1992 is a low input impedance current comparator that has led to broader use of the structure. The proposed circuit reduces the propogation delay by reducing the input capcitance through having the input current at the source of M_1 and M_2 .

If the sum of I_{in} and the reference current applied to the comparator is positive, V_1 goes high and is amplified by M_2 and M_4 (here we assume M_1 has initially turned on). M_5-M_8 are just two inverters used to give a rail to rail output voltage

TABLE I TRANSISTOR SIZING

	Transistor	W/L
Current	M_1, M_4, M_{6-7}	0.88/0.36
Comparator	M_2, M_3, M_8	0.48/0.36
	$ m M_{5}$	4.0/0.36
SR Latch	M_1 - M_4	0.28/7.0
	$ m M_5 ext{-}M_8$	0.8/7.0
XOR Gate	M_1 - M_3 - M_5	4.0/1.0
	$\mathrm{M}_2 ext{-}\mathrm{M}_4 ext{-}\mathrm{M}_6$	2.0/1.0
Voltage	$M_{1-2}, M_{5-6}, M_{10-13}, M_{16-17}, M_{20}$	1.0/0.5
Comparator	$M_{3-4}, M_7, M_{14-15}, M_{19}$	2.5/0.5
	M_{8-9}, M_{18}	1.5/0.5

signal. Based on current direction to the comparator, the gate of M_5 , M_7 would have either a low or high impedance path to ground translated by the two inverters to a low or high voltage, respectively. When the input of the inverters is a high impedance node, and with the gate of the inverters drawing almost zero current, the voltage is close to the voltage connected to the input current (VDD) which causes a high voltage at the output of the second inverter. Using the two inverters facilitate connection of this voltage signal to the next stage while mitigating loading effects.

C. SR-Latch, XOR, and Voltage Comparator With Rail to Rail Swing

A CMOS NAND gate based SR-latch is used as the output stage of the impedance to frequency system. In this design, transistors are sized to operate with extremely low power of 3 nW and are fast enough to be compatible with the switching rate of 10 MHz. The designed SR-latch is shown in Fig. 2(c) and the XOR circuit is shown in Fig. 2(d). The comparator circuit is shown in Fig. 2(e). M_1-M_4 is preamplifier stage, $M_{10}-M_{13}$ enhances the decision by positive feedback from the cross coupled devices, and $M_{14}-M_{18}$ is the post amplifier circuit. All transistor sizes is shown in Table I. The transistors are sized for low power consumption.

D. Transmitter and Receiver

In order to transfer the output signal for remote further processing, the commercially available Quasar UK FM hybrid transmitter module is used. The module is very simple to setup, does not need additional parts to operate and offers low current consumption (typ. 1 mA). Data can be supplied directly from CMOS/TTL devices and has a low hardware cost (\$ 6). The low current consumption, allows for extended battery life when used in mobile applications. The FM transmitter is depicted in Fig. 2(f) and the receiver block can be seen in Fig. 5. In comparison to RF module used in [15], [16], this RF transmitter uses 10 times less power, is smaller and does not require a micro-controller to send or data. The receiver system is flexible to setup, in our setup the receiver was connected to an Arduino board and the received data was communicated to a laptop trough serial communication. The Arduino is used primarily for ease of use in connecting the receiver to the laptop.

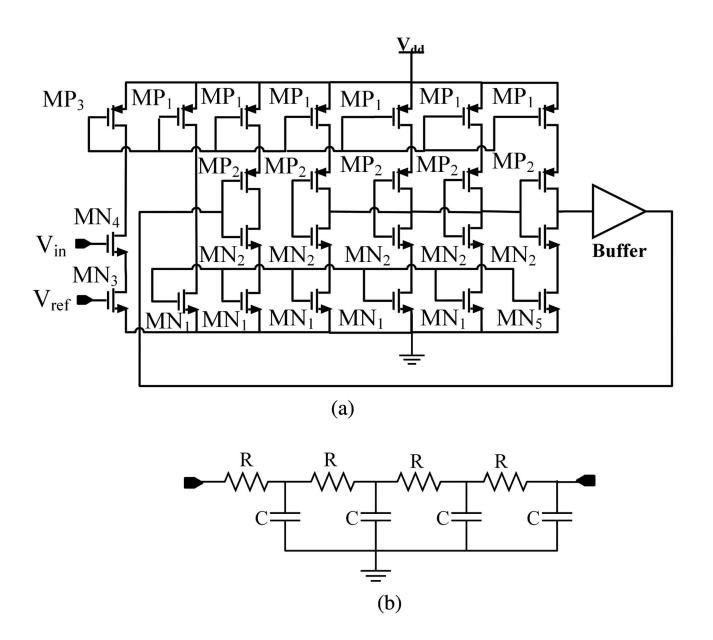


Fig. 4. (a) On-chip current starved VCO and (b) RC filter to generate a sine wave.

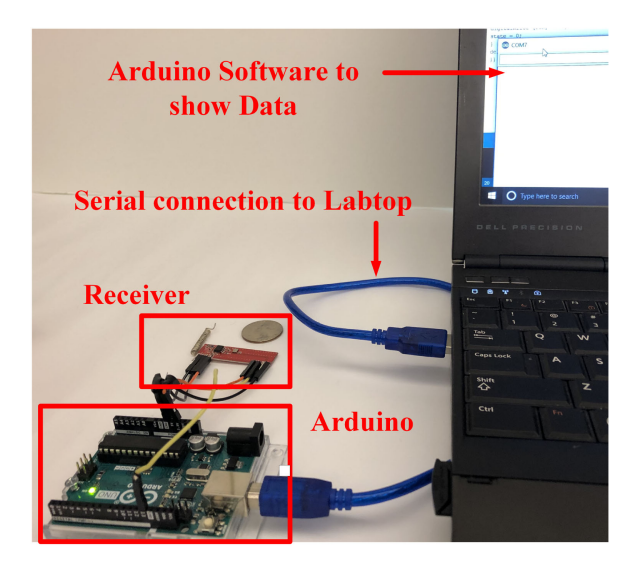


Fig. 5. FM receiver setup with Arduino.

III. SIMULATED AND EXPERIMENTAL RESULTS

The designed impedance measurement system was tested both through simulation and experiment to confirm the functionality of the circuit. In the experiments without the on-board sinusoidal generator circuit, a Hewlett Packard, 33120 A waveform generator is used to generate an ideal stimulating sinusoidal signal. An Agilent E3831 A is used to supply the DC voltages, and all signals are recorded using Agilent technologies-X3104 Storage Oscilloscope. To generate the sinusoidal signal on the system boards, two options were tested, a discrete XR2206 and on-chip VCO with discrete filter is used. The XR2206 increase the overall system area by 4 cm^2 and consumes 80 mA of power consumption. The VCO is implemented in 180 nm, consumes 110 μ A and has the area of 0.04 mm^2 . The VCO based sinusoidal voltage generator system with discrete buffer

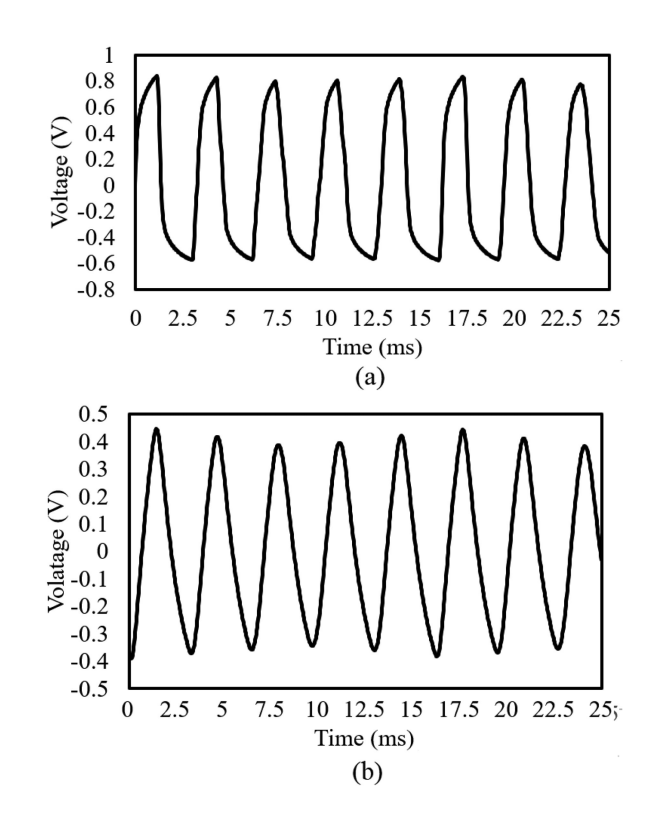


Fig. 6. Experimental measurements of (a) output of the VCO before the RC filter, showing a signal with a distortion and (b) sinusoidal voltage after the RC filters and the buffer with the impedance sensor connected to it.

and RC filter increases the power consumption to 240 μ A and the size by 2 cm^2 . Fig. 6 (a) shows the output of the VCO before the RC filter, Fig. 6 (b) shows the sinusoidal voltage after the RC filters and the buffer with the impedance sensor connected.

1) Resistance sensor:

As noted in section II, the first block of the resistance measurement system is a current comparator. The simulation results of the current comparator is depicted in Fig. 7. For doing the DC characteristics of the current comparator, in Fig. 7(a), we connected a 6 μ A on one input and swept 4 to 8 μ A on the other. This showed an output change of GND to VDD on 6 μ A. In Fig. 7(b) the positive input is swept from 4 to 8 μ A, while the negative input is stepped from 4 to 8 μ A in 1 μ A increments. As shown in Fig. 7(a), the offset is about 0.2 μ A. The derivative of this plot shows the gain of this comparator (Fig. 7(c)) which is about 4 M.

For comparison, a constant current and a sinusoidal reference were used as the inputs. As depicted in Fig. 8, the output pulse is low when the input current is lower than the reference and is high when the input current is higher than the reference. The plot is shown for 1 μ A and 8 μ A.

To test the circuit experimentally, a sinusoidal voltage source with a 0.5 V amplitude and frequency of 1 kHz was used as one input and the other input was a changing DC voltage. Both inputs went through 5 K resistors to generate current. The transient response of the circuit is shown in Fig. 9. In Fig. 10, the output is tested for different values of resistance which confirm the linearity of the impedance measurement circuit over a large

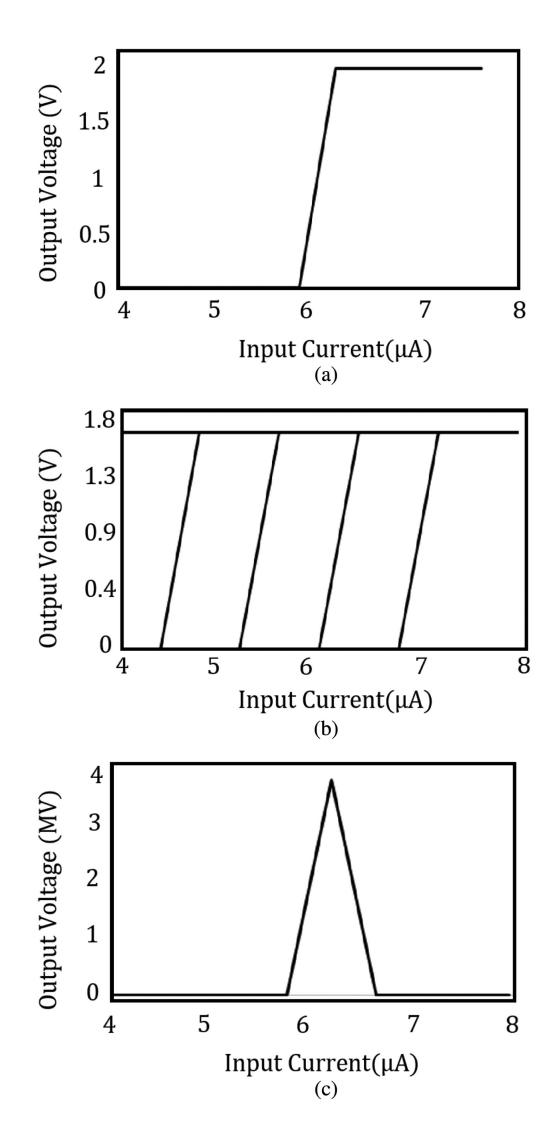


Fig. 7. Simulated current comparator characterization using DC sweep. (a) Current comparator having 6 μ A on one input and a sweeping 4 to 8 μ A on the other, showing and output change of GND to VDD on 6 μ A. (b) Positive input is swept from 4 to 8 μ A, while the negative input is stepped from 4 to 8 μ A in 1 μ A increments. (c) Gain of the current comparator.

range. Published values for the resistances range from 10^2 to $10^5~\Omega cm^2$, with most around 1 k Ωcm^2 , and as seen in Fig. 10, our circuit is functional in this range. The capacitance is usually given as around $0.1~\mu F/cm^2$, with published data between 0.1 and 1 $\mu F/cm^2$. As a separate test, the capacitance was set to a low value (1 pF) and to a high value (10 μ F) to determine if the system could detect a faulty connection to the skin. Under these conditions, the resistance measurement changed to a flat line.

To change a pulse width to the high frequency pulse train, a reference with a larger frequency and an SR-latch was chosen to modulate the pulse-width. The next block tested experimentally is the SR-latch. The output of the SR-latch is shown in Fig. 11. When the set signal is high, the output is high and when the reset is high, the latch is reset. This block was tested with VDD a low as 0.5 V to show the functionality of latch even with small changes. In our design, the time reference used was 10 MHz. Here the pulse frequency at the output is correlated with the

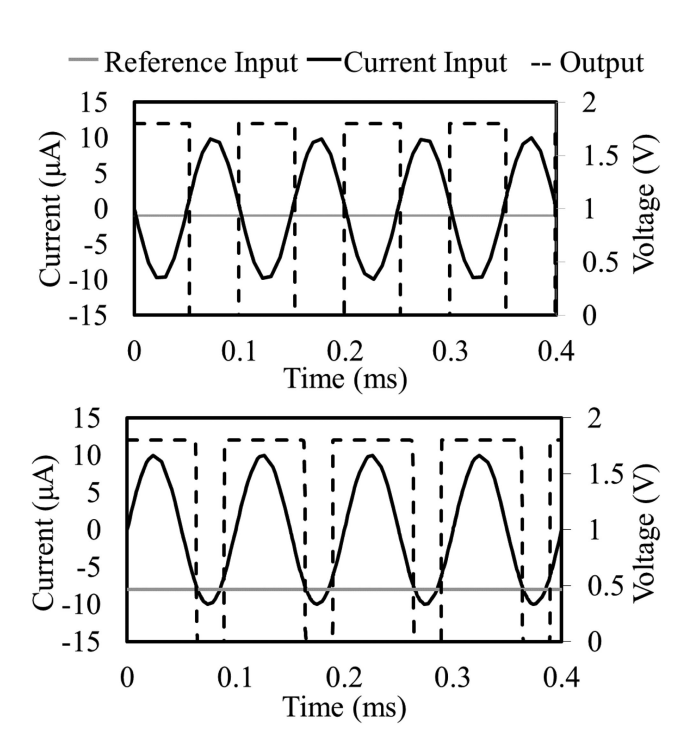


Fig. 8. Current comparator simulation output for a changing sinusoidal input compared to a constant DC current input for 2 different reference currents.

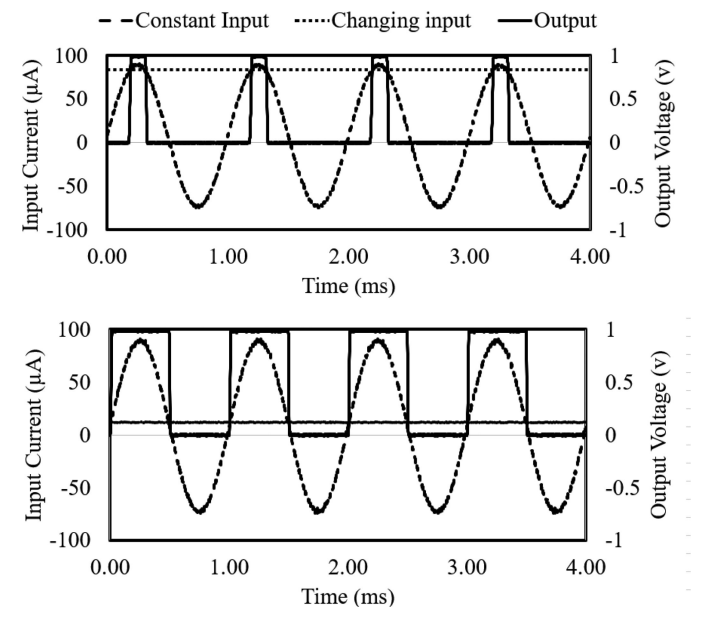


Fig. 9. Transient response for experimental impedance measurement for 2 different currents.

pulse width of the input signal. With a wider pulse width, there is an increased number of pulses of fixed width and lower pulse width means decreased number of pulses with fixed width. The accuracy of the system can be increased if a higher frequency is used as the SR-latch reference.

To see the linearity of our system, the output frequency was measured for $10~\Omega$ to $10~k\Omega$ input impedance at every $1~k\Omega$. The experimental results are shown in Fig. 12.

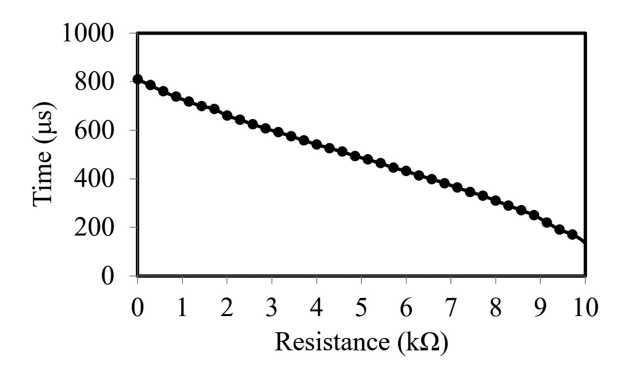


Fig. 10. Experimental measurement for different system output pulse width for difference impedance showing linear duty-cycle with decrease in impedance.

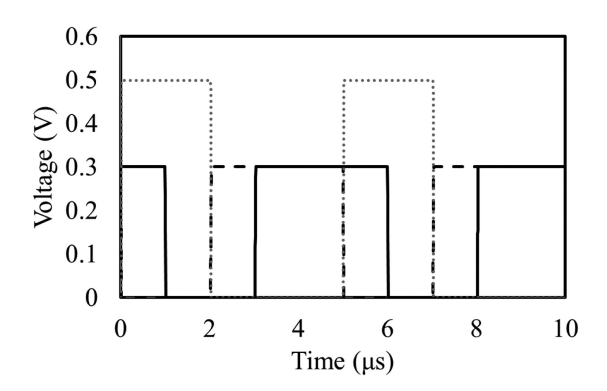


Fig. 11. Experimental SR-latch output showing high output when set signal is high, and low output when reset is high.

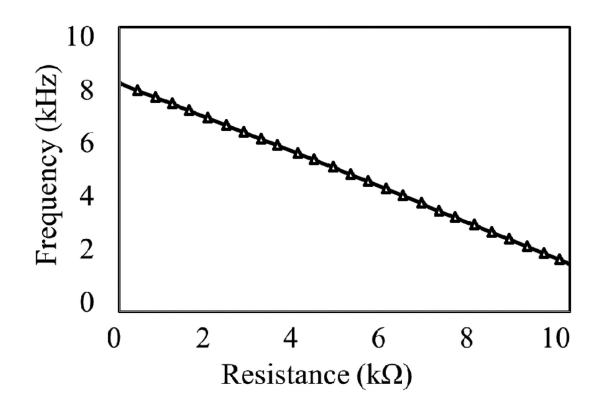
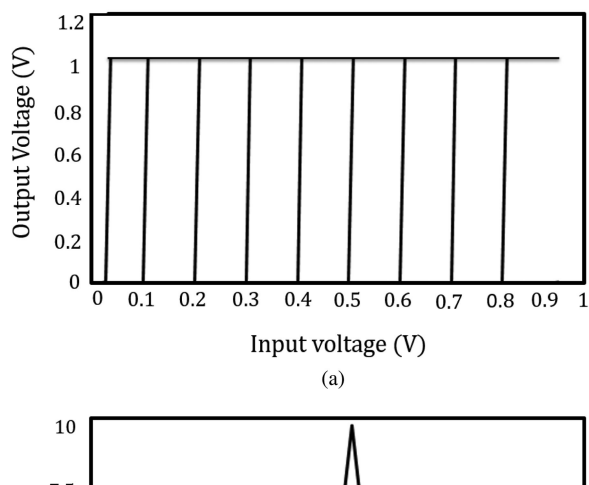


Fig. 12. Experimental system output frequency for 10 Ω to 10 $k\Omega.$

2) Capacitance Sensor: To test the capacitance measurement system, the reference AC stimulating signal is passed through a reference resistance and an impedance that consists of resistance and capacitance. Since the signal going through a capacitive element changes the phase, voltage comparators can be used to detect a constant voltage crossing.

For doing the DC characteristics in the voltage comparator (Fig. 13(a)), the positive input is swept from 0 to 1 V while the negative input is stepped from 0-1 V in 100 mV increments. The derivative of this plot shows the gain of this comparator (Fig. 13(b)). As shown in the plot, A is approximately 10,000. This change in phase is converted to duty cycle using an XOR gate. To see the linearity of the system, the output frequency was



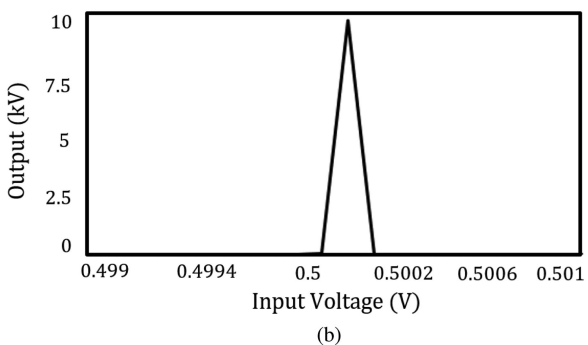


Fig. 13. Simulated voltage comparator characterization using DC sweep. (a) Positive input is swept from 0 to 1 V while the negative input is stepped from 0-1 V in 100 mV increments. (b) Gain of the current comparator.

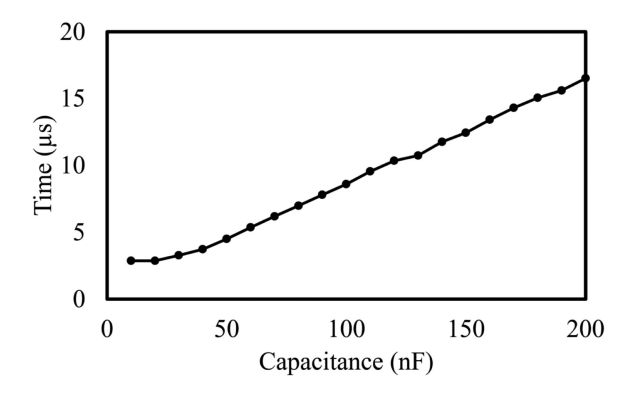


Fig. 14. Experimental system output pulse width for different capacitances.

measured for $10~\rm nF$ to $200~\rm nF$ input capacitance at every $10~\rm nF$. The simulation results are shown in Fig. 14.

To test the capacitance measurement system, the reference AC stimulating signal is passed through a reference resistance and an impedance that consists of resistance and capacitance. Fig. 15 shows the transient response for 100 nF that has a duty cycle of 90 μ s. The duty cycle was also recorded for 50 nF and 33 nF that showed the duty cycle of 45 μ s and 30 μ s respectively. The system layout was done in 180 nm CMOS technology. It can be seen from Fig. 16 that the total area of the system does not exceed 300 μ m². Fig. 17(a) and Fig. 17(b) show the result of measuring a complex impedance. In Fig. 17(a) resistance measurement is done while having 3 different capacitance, and in Fig. 17(b) capacitance is measured while having 3 different

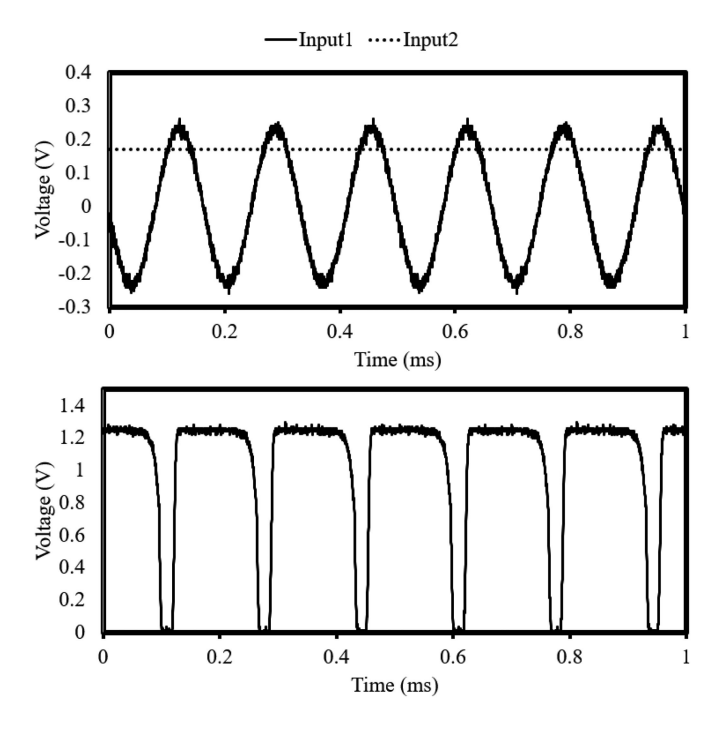


Fig. 15. Experimental transient response for 100 nF experimental impedance measurement.

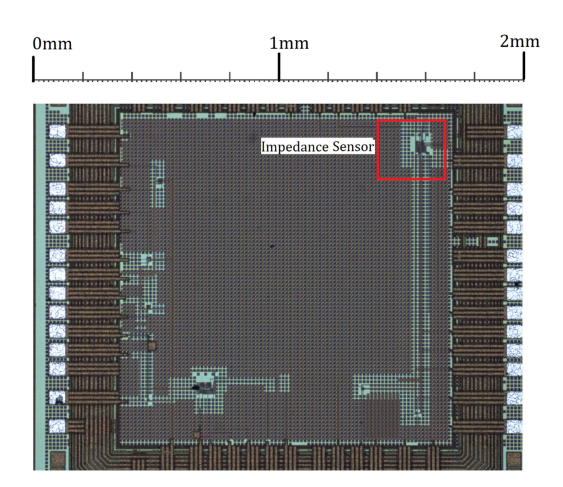


Fig. 16. Fabricated impedance to frequency photomicrograph.

resistance. This shows an ignore-able counter measurement while having complex measurement. Since a non-ideal signal generator may contribute error to the impedance measurement, Fig. 17 also shows the capacitance and resistance measurement for the discrete function generator and VCO based function generator for the 5 passive loads (triangle and circles respectively). The measurements done with the two latter non-ideal sources is subtracted from the measurement done with the function generator and the value is divided by the resistor/capacitor value and averaged. Based on this, the resistor measurement had an error of 5% and the capacitance measurement had an error of 7% using the VCO based circuit.

The noise measurement was done using SR785 showing an average noise density of 12 μ V/Hz in the 10 Hz to 100 kHz frequency range. The sensor's sensitivity is a function of the

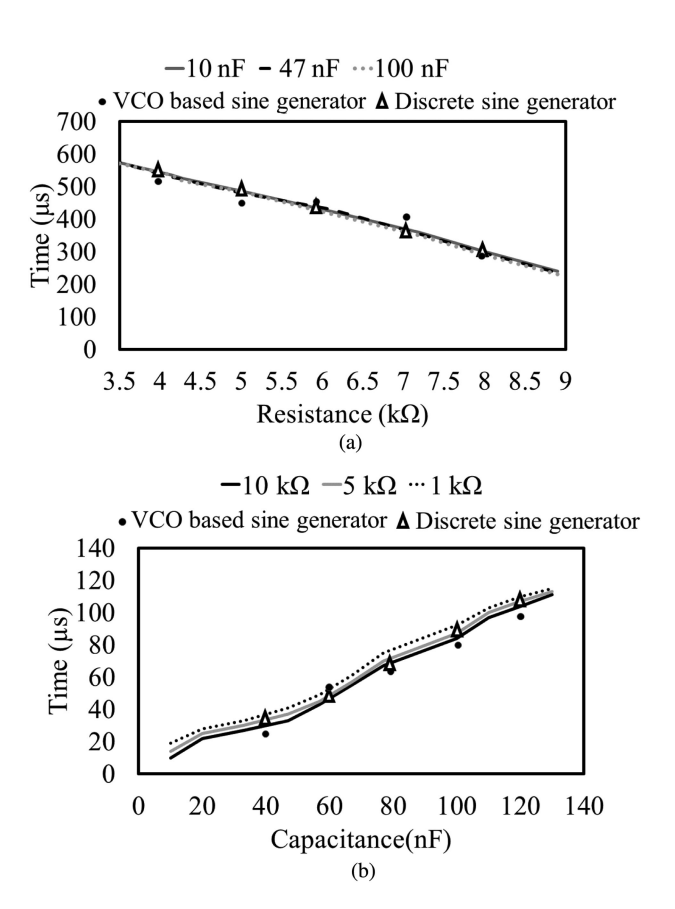


Fig. 17. Experimental RC simultaneous measurement showing (a) Resistance measurement for 3 different capacitances. A small change in resistance measurement with 3 capacitance values, 10 nF, 47 nF, 100 nF. (b) Capacitance measurement for 3 different resistances. A small change in capacitance measurement with 3 resistance values, 1 k Ω , 5 k Ω , 10 k Ω . (Lines are derived using a benchtop signal generator for the exciting signal).

SR-latch reference input, making the resolution of the system tunable. To be compliant with the transmitter frequency rate (433 MHz) the signal reference was chosen 10 MHz, switching up to 1000 times in the 1 ms bandwidth of the signal. Each output pulse of the output stage of SR-latch is therefore associated to 0.5 Ω of impedance change. If the stimulating sinusoidal frequency is increased by ten, with the same SR-latch frequency of 10 MHz, each pulse of the SR latch corresponds to 10 Ω and the system will still be functional but with the resolution reduced from 1 Ω to 10 Ω .

3) PCB Fabrication: The PCB was then fabricated using Express PCB which is illustrated in Fig. 2(f). The system depicted can be connected to chest for Trans-thoracic impedance measurement (first application). The trans-thoracic system is shown in Fig. 18. For hand gesture recognition (second application) it is developed using adhesive copper tape and 16 1.5 cm ×1 cm electrodes were made on a velcro strap. Fig. 19 shows the system on wrist. To reduce the error, the same size of electric paint is put on the wrist. Our fabricated PCB uses a coin battery to power up the whole system and a MAX 863DS, a dual, high-efficiency, DC-DC controller is used to supply the chip voltage. The MAX 863DS is cheap and can supply adjustable voltage as low as 1 V using 2 feedback resistors marked on the PCB as FB1 and FB2.



Fig. 18. Impedance measurement system, with conductive electrodes, placed on skin using medical tape to measure the impedance.



Fig. 19. Hand gesture recognition system.

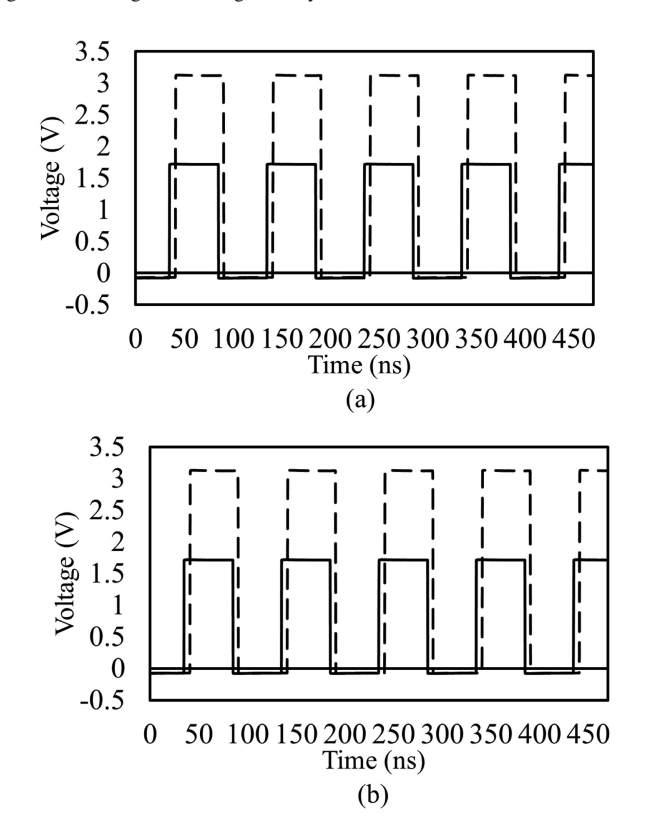


Fig. 20. Experimental input signal to transmitter and signal received at the receiver (a) 30 cm and (b) 1.5 m away shows number of pulses stays the same. The number of pulses is then counted and impedance information is extracted.

TABLE II
HUMAN EXPERIMENTS DONE 5 TIMES IN A DAY EVERY 3 HOURS SHOWING
MEASURED RESISTANCE, CAPACITANCE AND STANDARD DEVIATION

	Resistance	Deviation	Capacitance	Deviation
	(Ω)	(Ω)	(nF)	(nF)
Benchtop System	110		108	
	114		110	
	115		108	
Male Subject	112	1.2	108	2
	114		112	
	112		106	
Benchtop System	100		101	
	100		102	
	104		105	
Female Subject	101	1.6	104	1.75
	101		102	
	104		100	

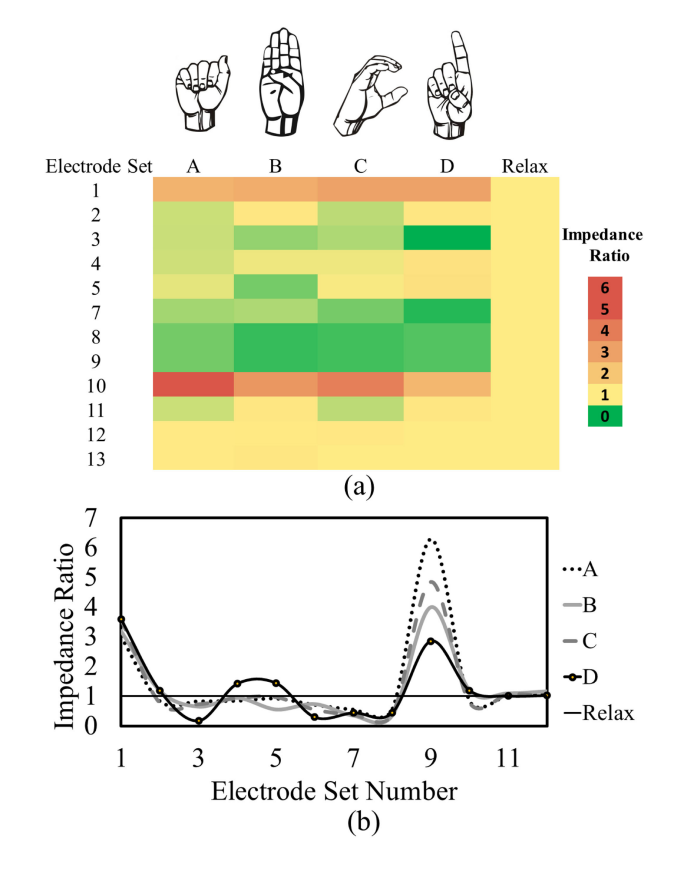


Fig. 21. Experimental hand gesture recognition results showing the impedance of sign language letter A-D. The impedance is measured in ratio to relax status in (a) heat map (b) line plot.

Another advantage of the MAX 863DS is its low-battery Output (LBO), an open-drain N-channel MOSFET output that is connected to ground when the voltage on low-battery comparator input (LBI) drops below 1.25 V. To use this function the LBI pin is set to 1.25 V, therefore when the battery voltage drops lower than 1.25 V, LBO is connected to ground. A low power SMD LED is connected to this pin, in series with a resistor and connected to battery so that it indicates the need to change the battery when it turns on. The signal is then modulated and sent by the transmitter. The transmitted and received signal for a constant resistance is shown in Fig. 20, the transmitter was

	Application	Range	Sensitivity	Hardware	Power	Size	Weight	Data
		(Ω)	Resolution	Implementation	(mw)	$(mm \times mm)$	(g)	Transfer
[15]	Tissue Impedance	1-54	0.5 Ω	Discrete	14	48×30	N/A	RF module
								2.4GHz nRF24L01
[23]*	Biomedical Impedance	100	0.15 Ω	65nm	0.01	3.55×1.36	N/A	None
[25]	Thoracic Impedance	50-400 m	0.1 Ω	$0.18\mu\mathrm{m}$	3.9	150×150	N/A	SRAM
[28]	Trans-thoracic Bioimpedance	10-20	3 Ω	Discrete	546	145×40	30	Bluetooth
[43]	Impedance Tomography	1-10k	8.8 Ω	$0.35 \mu { m m}$	100	N/A	N/A	N/A
[61]	Trans-thoracic Impedance	10-40	1m Ω	Discrete	120	38×18	70	Serial
[62]	Impedance Cardiography	1-1k	0.1 Ω	Discrete	406	85×65	200	Bluetooth
[63]*	Tissue Impedance	1k-100k	3 Ω	$0.18 \mu { m m}$	0.01	4.3×5	N/A	None
This Work	Trans-thoracic Impedance	1-10k	1 Ω	$0.13 \mu { m m}$	3.24**	45×25	12.3	RF module
								433MHz QAM-TX2

TABLE III
COMPARISON WITH STATE OF THE ART TRANS THORACIC SYSTEMS

^{*} This design is not a whole system but an impedance sensing chip without a means of data transfer. ** This includes the power for VCO based sine wave generator and all discrete modules

	Sensor	Measurement	Electrode #	Gesture #	Supply	Power	Electrode	Data
	Jensor	Device	Zieediode //	Gestare //	(V)	(mW)	Size (mm × mm)	Transfer
[33]	EIT	Discrete, AD5930	16/32	Any	3.3	50	3.4 × 15.3	Wire
[34]	Air	Data Acquisition	6	4	-	625	35 ×45	WiFi
	pressure	Board						
[35]	Strain	Discrete	4	8	5	-	0.7×10	WiFi
[36]	Capacitive	Discrete, ATSAM3X8E	5	6	3.3	450	20 ×20	Wire
[37]	EIT	Discrete, AD8250	8	Any	5	20	-	UART
[38]	EIT	Partially integrated	8	13	3.3	20	-	UART
		Discrete DAC						
[39]	EIT	Partially integrated	16	Any	12	600	25×5	UART
		Discrete DAC, AD9237						
This Work	Impedance	Integrated sensor	16	Any	3.3	0.6	15×10	RF module

TABLE IV

COMPARISON OF HAND GESTURE RECOGNITION SYSTEMS WITH STATE OF THE ART

tested both with 30 cm and 1.5 m distance from receiver, with no degradation of signal. The last stage of our circuit is an SR-latch that changes the pulse width to a high frequency pulse train. The pulse width associated with the resistance or capacitance measured is coded in the number of pulses. Since the data is coded to the number of pulses, receiver delay or the change of signal amplitude from chip level (1.8 V) to TTL (3 V) during transmission causes no problems.

4) Human Experiments: For human subject experiments, the recruitment and testing complied with the IRB code of conduct [61]. All the participants read and signed a consent form before entering the study. They were explained the process and could stop participating at any time. For the thoracic impedance measurement a male and female subject were tested. For the hand gesture recognition the system was tested on one female subject.

Thoracic Impedance: To the authors knowledge there are currently no FDA approved impedance sensors available for medical use to detect trans-thoracic impedance. In 2009 Corventis Inc. released an FDA cleared non-invasive, wireless cardiac monitor system [58]. This company was later acquired by Medtronics that change the device application to be an implantable cardiac monitor. There are other non FDA approved devices, like the Zenta watch from VINAYA [59] that could not be used for biomedical signal acquisition per human experiment code of conduct. Therefore to have a benchmark impedance for the impedance measurement for the thoracic impedance, an Agilent 4294 A precision impedance measurement analyzer is

used. The system was tested on a male and a female to prove the measurement remains constant in time for a healthy person. The signal is measured and calculated for 5 times in a 12 hour period and the average impedance along with standard deviation is shown in Table II.

For human measurements, the system shown in Fig. 18 was used. The electrodes were based on a nontoxic conductive electric paint The measured impedance for these electrodes were 33.7 Ω to 42.1 Ω (mean of 37.9 Ω and standard deviation of 4.2 Ω) in line with the expected 32 Ω/Square [60]. The motivation, design, and validation of the conductive paint based electrodes will be addressed in a future work.

Hand Gesture: The hand gesture recognition system was stabilized on the wrist using an adjustable Velcro tape. The 16 electrode and conductive paint dots on the wrist was placed and a stimulating signal was applied to each electrode pair. The impedance on the other electrode was then measured. The experiment was repeated 4 times for each gesture and for 5 different gestures. The results are shown in Fig. 21. When doing the experiment the stimulation 40 kHz sinusoidal signal is applied thorough two electrodes, for measurement the electrode adjacent to the stimulating electrode is ignored and all the other pairs are measured giving 13 measurements. In Fig. 21 (a) the results is shown in a heat map for letters A-D shown in sign language. For this experiment, the stimulation electrode is placed on the palm side, in the middle of the wrist where the main tendons lies. For a better presentation, impedance ratio to relax is shown in the figure. The impedance for the relax position is

therefore one and all the other impedances are compared to the relax position. It is observed that electrodes that are placed on the bone have a slighter change in different hand gestures. Fig. 21 (b) shows the pattern of impedance measured for different hand gesture. This data measurement is proof of concept that with data processing along with a simple predicting algorithms, gestures of sign language can be detected with a device with 30 μ W power consumption per channel. In our experiment, a single sensor was used which is switched amongst the electrodes. There are advantages and disadvantages to this approach. The primary advantage is power savings. Another advantage is eliminating cross talk between wires, compared to 13 simultaneous data transfer. The off-chip power management unit along with the sensor consumes 600 μ W. If separate impedance sensors were used for each electrode, there will be an additional 450 μ W power-consumption. Increased number of sensors will increase the accuracy and the speed of the recognition from 4 milliseconds to 0.25 milliseconds. The comparison of the designed sensor impedance measurement system to state of art with other systems used in biomedical application is shown in Table III and Table IV.

IV. CONCLUSION

In this paper, a low power compact impedance measurement system was demonstrated. The impedance sensing system is designed in a 0.18 μ m CMOS technology. The core sensors operate on 30 μ W for tissue impedance applications per channel and 600 μ W for the hand gesture with 16 electrodes. Assuming mass fabrication for the chip and PCB, the system cost is under \$10 and consumes 3 mW with the RF transmitter module. Using a 3 V coin battery the system can work for up to 140 hours without the need for standby mode or a pause in impedance sensing. The system weighs 10 grams and is 4.5 cm \times 2.5 cm big, making it suitable for connection to the body using adhesive medical tape and obviating the need for any king of strapping. The functionality of the system is tested with conductive paint on filter paper for accuracy. With the advancement of conductive paints in near future, the use of the system is possible without the need for medical electrodes and contact gels. To have a chip that is capable of sweeping the frequency, an automated means of sweeping this frequency could be added to the integrated circuit.

REFERENCES

- J. C. Mrquez, F. Seoane, and K. Lindecrantz, "Textrode functional straps for bioimpedance measurements-experimental results for body composition analysis," *Eur. J. Clin. Nutr.*, vol. 67, no. S1, pp. S22–S27, 2013.
- [2] A. Rao, E. K. Murphy, R. Halter, and K. Odame, "A 1 MHz miniaturized electrical impedance tomography system for prostate imaging," *IEEE Trans. Biomed. Circuits Syst.*, vol. 14, no. 4, pp. 787–799, Aug. 2020.
- [3] S. Rossi et al., "A low power bioimpedance module for wearable systems," Sensors Actuators, vol. 232, pp. 359–367, 2015.
- [4] D. Blanco-Almazán, W. Groenendaal, F. Catthoor, and R. Jané, "Chest movement and respiratory volume both contribute to thoracic bioimpedance during loaded breathing," Sci. Rep., vol. 9, pp. 1–11, 2019.
- [5] B. He et al., "Waveform analysis of differential graphs of reconstructed impedance cardiography from healthy individuals," Ann. Noninvasive Electrocardiol., vol. 25, 2020, Art. no. e12714.

- [6] K. Sel, B. Ibrahim, and R. Jafari, "ImpediBands: Body coupled bioimpedance patches for physiological sensing proof of concept," *IEEE Trans. Biomed. Circuits Syst.*, vol. 14, no. 4, pp. 757–774, Aug. 2020.
- [7] M. Min, P. Annus, H. Kiv, A. Krivoei, T. Uuetoa, and J. Lamp, "Bioimpedance sensing-a viable alternative for tonometry in non-invasive assessment of central aortic pressure," in *Proc. IEEE Int. Symp. Med. Meas.* Appl., 2017, pp. 373–378.
- [8] M. Zamani, Y. Rezaeiyan, O. Shoaei, and W. A. Serdijn, "A 1.55 μW bio-impedance measurement system for implantable cardiac pacemakers in 0.18 μm CMOS," *IEEE Trans. Biomed. Circuits Syst.*, vol. 12, no. 1, pp. 211–221, Feb. 2018.
- [9] X. Zhao, V. Sadhu, T. Le, D. Pompili, and M. Javanmard, "Toward wireless health monitoring via an analog signal compression-based biosensing platform," *IEEE Trans. Biomed. Circuits Syst.*, vol. 12, no. 3, pp. 461–470, 2018.
- [10] A. Choi et al., "Smartphone-based bioelectrical impedance analysis devices for daily obesity management," Sensors, vol. 15, no. 9, pp. 22151–22166, 2015.
- [11] F. Villa et al., "Wearable multi-frequency and multi-segment bioelectrical impedance spectroscopy for unobtrusively tracking body fluid shifts during physical activity in real-field applications: A preliminary study," Sensors, vol. 16, no. 5, p. 673, 2015.
- [12] J. Becher *et al.*, "Device-based impedance measurement is a useful and accurate tool for direct assessment of intrathoracic fluid accumulation in heart failure," *Europace*, vol. 12, no. 5, pp. 731–740, 2010.
- [13] W. Song et al., "Design of a wearable smart SEMG recorder integrated gradient boosting decision tree based hand gesture recognition," *IEEE Trans. Biomed. Circuits Syst.*, vol. 13, no. 6, pp. 1563–1574, Dec. 2019.
- [14] J. Ferreira, "Modular textile-enabled bioimpedance system for personalized health monitoring applications," Doctoral Dissertation, KTH Royal Institute of Technology, 2017.
- [15] S. Lee et al., "A low-power and compact-sized wearable bio-impedance monitor with wireless connectivity," in J. Phys.: Conf. Series, vol. 434, no. 1, 2013, Art. no. 012013.
- [16] S. Lee et al., "Congestive heart failure patient monitoring using wearable bio-impedance sensor technology," *IEEE Eng. Med. Biol. Soc. Conf.*, 2015, pp. 438–441.
- [17] J. Ramos, J. L. Ausn, A. M. Lorido, F. Redondo, and J. F. Duque-Carrillo, "A wireless, compact, and scalable bioimpedance measurement system for energy-efficient multichannel body sensor solutions," *J. Phys.: Conf. Series*, vol. 434, no. 1, 2015, Art. no. 012016.
- [18] B. Riegel, S. L. Christopher, and V. V. Dickson, "Self care in patients with chronic heart failure," *Nat. Rev. Cardiol.*, vol. 8, no. 11, pp. 644, 2011.
- [19] L. Wang, "Fundamentals of intrathoracic impedance monitoring in heart failure," Amer. J. Cardiol., vol. 99, no. 10, pp. S3-S10, 2007.
- [20] J. P. Auld and C. S. Lee, "Changes in heart failure self-care behaviors and intrathoracic impedance over 6 months," *J. Cardiac Failure*, vol. 24, no. 8, p. S7, 2018.
- [21] D. Catanzariti et al., "Monitoring intrathoracic impedance with an implantable defibrillator reduces hospitalizations in patients with heart failure," Pacing Clin. Electrophysiol., vol. 32, no. 3, pp. 363–370, 2009.
- [22] V. M. Conraads et al., "Sensitivity and positive predictive value of implantable intrathoracic impedance monitoring as a predictor of heart failure hospitalizations: The SENSE-HF trial," Eur. Heart J., vol. 32, no. 18, pp. 2266–2273, 2011.
- [23] K. Kim *et al.*, "22.3 A 0.5 V 9.26 μ W 15.28 m Ω Hz bio-impedance sensor IC with 0.55° overall phase error," in *Proc. IEEE Int. Solid-State Circuits Conf.*, 2019, pp. 364–366.
- [24] R. M. Khandwalla, K. Birkeland, R. Zimmer, M. Banet, S. Pede, and I. Kedan, "Predicting heart failure events with home monitoring: Use of a novel, wearable necklace to measure stroke volume, cardiac output and thoracic impedance," *J. Amer. College Cardiol.*, vol. 67, no. 13 Supplement, p. 1296, 2016.
- [25] L. Yan, J. Bae, S. Lee, T. Roh, K. Song, and H. J. Yoo, "A 3.9 mW 25-Electrode reconfigured sensor for wearable cardiac monitoring system," *IEEE J. Solid-State Circuits*, vol. 46, no. 1, pp. 353–364, Jan. 2010.
- [26] J. C. Marquez, "On the feasibility of using textile electrodes for electrical bioimpedance measurements," Ph.D. Dissertation, Stockholm: Skolan fr Teknik och Hlsa, Kungliga Tekniska Högskolan, Stockholm, Sweden, 2011.
- [27] M. Ulbrich et al., "The IMPACT Shirt: Textile Integrated and Portable Impedance cardiography," Physiol. Meas., vol. 35, no. 6, p. 1181, 2014.
- [28] T. Schlebusch, L. Rothlingshofer, S. Kim, M. Kny, and S. Leonhardt, "On the road to a textile integrated bioimpedance early warning system for lung edema," in *Proc. Int. Conf. Body Sensor Netw.*, 2010, pp. 302–307.

- [29] F. Seoane, J. C. Marquez, J. Ferreira, R. Buendia, and K. Lindecrantz, "The challenge of the skin-electrode contact in textile-enabled electrical bioimpedance, measurements for personalized healthcare monitoring applications," *Biomed. Eng.*, pp. 541–546, 2011.
- [30] M. M. Mellenthin et al., "The ACE1 electrical impedance tomography system for thoracic imaging," *IEEE Trans. Instrum. Meas.*, vol. 68, no. 9, pp. 3137–3150, Sep. 2019.
- [31] K. Sridevi, M. Sundarambal, K. Muralidharan, and R. L. Josephine, "FPGA implementation of hand gesture recognition system using neural networks," in *Proc. Int. Conf. Intell. Syst. Control*, 2017, pp. 34–39.
- [32] Y. Zhang and C. Harrison, "Tomo: Wearable, low-cost electrical impedance tomography for hand gesture recognition," in *Proc. Annu. ACM Symp. User Interface Softw. Technol.*, 2015, pp. 167–173.
- [33] Y. Zhang, R. Xiao, and C. Harrison, "Advancing hand gesture recognition with high resolution electrical impedance tomography," in *Proc. Annu. Symp. User Interface Softw. Technol.*, 2016, pp. 843–850.
- [34] P. G. Jung, G. Lim, S. Kim, and K. Kong, "A wearable gesture recognition device for detecting muscular activities based on air-pressure sensors," *IEEE Trans. Ind. Informat.*, vol. 11, no. 2, pp. 485–494, Apr. 2015.
- [35] A. Ferrone et al., "Wearable band for hand gesture recognition based on strain sensors," in Proc. IEEE Int. Conf. Biomed. Robot. Biomechatron., 2016, pp. 1319–1322.
- [36] X. Liang, H. Heidari, and R. Dahiya, "Wearable capacitive-based wrist-worn gesture sensing system," in *Proc. New Generation CAS*, 2017, pp. 181–184.
- [37] Y. Wu, D. Jiang, J. Duan, X. Liu, R. Bayford, and A. Demosthenous, "Towards a high accuracy wearable hand gesture recognition system using EIT," in *Proc. IEEE Int. Symp. Circuits Syst.*, 2018, pp. 1–4.
- [38] Y. Wu, D. Jiang, X. Liu, R. Bayford, and A. Demosthenous, "A human-machine interface using electrical impedance tomography for hand prosthesis control," *IEEE Trans. Biomed. Circuits Syst.*, vol. 12, no. 6, pp. 1322–1333, Dec. 2018.
- [39] D. Jiang, Y. Wu, and A. Demosthenous, "Hand gesture recognition using three-dimensional electrical impedance tomography," *IEEE Trans. Circuits Syst. II*, vol. 67, no. 9, pp. 1554–1558, Sep. 2020.
- [40] A. Hedayatipour, S. Aslanzadeh, and N. McFarlane, "CMOS integrated impedance to frequency converter for biomedical applications," in *Proc. IEEE Int. Symp. Circuits Syst.*, Spain, Oct. 2020.
- [41] A. Hedayatipour, S. Aslanzadeh, and N. McFarlane, "CMOS based whole cell impedance sensing: Challenges and future outlook," *Biosensors Bioelectron.*, 2019, Art. no. 11600.
- [42] A. Mucha, M. Schienle, and D. Schmitt-Landsiedel, "Sensing cellular adhesion with a CMOS Integrated Impedance-to-frequency Converter," in *Proc. Sensors Appl. Symp.*, 2011, pp. 12–17.
- [43] P. Vooka and B. George, "A direct digital readout circuit for impedance sensors," *IEEE Trans. Instrum. Meas.*, vol. 64, no. 4, pp. 902–912, Apr. 2014.
- [44] D. Allegri, A. Donida, P. Malcovati, and D. Barrettino, "CMOS-based multi frequency impedance analyzer for biomedical applications," *IEEE Trans. Biomed. Circuits Syst.*, vol. 12, no. 6, pp. 1301–1312, Aug. 2018.
- [45] T. Chen, W. Wu, C. Wei, R. B. Darling, and B. Liu, "Novel 10-bit impedance to-digital converter for electrochemical impedance spectroscopy measurements," *IEEE Trans. Biomed. Circuit Syst.*, vol. 11, no. 2, pp. 370–379, Apr. 2017.
- [46] H. Jafari, L. Soleymani, and R. Genov, "16-channel CMOS impedance spectroscopy DNA analyzer with dual-slope multiplying ADCs," *IEEE Trans. Biomed. Circuits Syst.*, vol. 6, no. 5, pp. 468–478, Oct. 2012.
- [47] X. Liu, D. Rairigh, C. Yang, and A. J. Mason, "Impedance-to-digital converter for sensor array microsystems," in *Proc. Int. Symp. Circuits Syst.*, 2009, pp. 353–356.
- [48] C. Yang and A. J. Mason, "Membrane protein biosensor with multi-channel CMOS impedance extractor and digitizer," in *Proc. IEEE Sensors*, 2008, pp. 642–645.
- [49] A. Ali, N. Pal, and P. M. Levine, "CMOS impedance spectroscopy sensor array with synchronous voltage-to-frequency converters," in *Proc. Int. Midwest Symp. Circuits Syst.*, 2015, pp. 1–4.
- [50] Wikimedia Commons, "Surface Anatomy of the Heart," [Online]. Available: https://commons.wikimedia.org/wiki/File:Surfaceanatomyof theheart.png, Accessed: May 2020.
- [51] S. F. Yalin et al., "Single-frequency and multi-frequency bioimpedance analysis: What is the difference?" Nephrol. (Carlton), vol. 23, no. 5, pp. 438–445, 2018.
- [52] D. Rairigh, Xiaowen Liu, C. Yang, and A. J. Mason, "Sinusoid signal generator for on-chip impedance spectroscopy," in *Proc. IEEE Int. Symp. Circuits Syst.*, 2009, pp. 1961–1964.

- [53] S. Hong and D. Jee, "A 0.052 mm², <0.4% THD, sinusoidal current generator for bio-impedance measurement using a recursive digital oscillator and current-domain FIR filter," *IEEE Trans. Circuits Syst. II: Exp. Briefs*, vol. 66, no. 6, pp. 894–898, Jun. 2019.
- [54] EXAR Corporation, "Monolithic Function Generator," XR2206 datasheet, Feb. 2008.
- [55] X. Wang, "Circuit blocks design for a current-mode CMOS image sensor chip," Ph.D. Dissertation, University of Victoria, 2010.
- [56] H. Traff, "Novel approach to high speed CMOS current comparators," IEEE Electron. Lett., vol. 28, no. 3, pp. 310–312, 30 Jan. 1992.
- [57] A. H. England and T. L. Clare, "Synthesis and characterization of flexible hydrogel electrodes for electrochemical impedance measurements of protective coatings on metal sculptures," *Electroanalysis*, vol. 26, no. 5, pp. 1059–1067, 2014.
- [58] "Corventis Launches AVIVO Mobile Patient Management System," 2015. [Online]. Available:https://www.dicardiology.com/product/corventis-launches-avivo-mobile-patient-management-system
- [59] S. Charara, "ZENTA: Stress & Emotion Management On Your Wrist," 2016. [Online]. Available: https://www.indiegogo.com/projects/zentastress-emotion-management-on-your-wrist/
- [60] "What is the Resistance of Electric Paint?" [Online]. Available: https://faqs.bareconductive.com/hc/en-gb, Accessed: Jan. 2020.
- [61] D. Jung, M. Adam, V. Dorner, and A. Hariharan, "A practical guide for human lab experiments in information systems research," J. Syst. Inf. Technol., pp. 228–255, 2017.
- [62] J. Ferreira, F. Seoane, and K. Lindecrantz, "Portable Bioimpedance monitor evaluation for continuous impedance measurements. towards wearable plethysmography appl.," in *Proc. IEEE Eng. Med. Biol. Soc. Conf.*, 2013, pp. 559–562.
- [63] A. Hafid, S. Benouar, M. Kedir-Talha, F. Abtahi, M. Attari, and F. Seoane, "Full impedance cardiography measurement device using rasp-berry pi3 and system-on-chip biomedical instrumentation solutions," *IEEE J. Biomed. Health Informat.*, vol. 22, no. 6, pp. 1883–1894, 2017.
- [64] C. W. Huang, C. H. Chung, R. S. Syu, and C. Y. Wu, "The design of CMOS electrode-tissue impedance measurement circuit using differential current switch with CMFB Bias for implantable neuro-modulation SoCs," in *Proc. IEEE Biomed. Circuits Syst. Conf.*, 2019, pp. 1–4, 2019.



Ava Hedayatipour (Member, IEEE) received the B.S. degree in electrical engineering from the Iran University of Science and Technology, Tehran, Iran, in 2012, and the M.S. degree in electrical engineering from Shahid Rajaee Teacher Training University, Tehran, Iran, in 2015. Since 2016, she has been working toward the Ph.D. degree with the Department of Electrical Engineering, University Tennessee Knoxville, Knoxville, TN, USA, as a Research and Teaching Assistant. Her current research interests include analog integrated circuit designs,

bioimplantable and biomedical devices, low-power and low-noise designs, microelectronics, mixed signal VLSI designs, and semiconductor devices.



Shaghayegh Aslanzadeh (Member, IEEE) received the B.S. and M.S. degrees in electrical engineering from Shahid Rajaee Teacher Training University, Tehran, Iran, in 2013 and 2015, respectively. She is currently working toward the Ph.D. degree in electrical engineering with the University of Tennessee, Knoxville, TN, USA. From August 2017, she has been a Research and Teacher Assistant with the Department of Electrical Engineering, University of Tennessee. Her research interests include the analog integrated circuit designs, bioimplantable and

biomedical devices, low-power and low-noise designs, microelectronics, mixed signal VLSI designs, and semiconductor devices.



Shahram Hatefi Hesari (Graduate Student Member, IEEE) received the B.S. degree in electrical engineering from Shiraz University, Shiraz, Iran and the M.S. degree in electrical engineering from Amirkabir University of Technology - Tehran Polytechnic, Tehran, Iran. He is currently working toward the Ph.D. degree and Graduate Teaching and Research Assistant with the Department of Electrical Engineering and Computer Science, University of Tennessee, Knoxville, TN, USA. His research interests includes biosensors and biomedical device applications, low-

power integrated circuit design, analog/mixed-signal integrated circuit design, RF microelectronics, monolithic sensors, nanotechnology and molecular scale electronics, semiconductor device modeling, and biomicroelectronics.



Nicole McFarlane (Senior Member, IEEE) received the B.S. and M.S. degrees in electrical engineering from Howard University, Washington, DC, USA, in 2001 and 2003, respectively, and the Ph.D. degree in electrical engineering from the University of Maryland, College Park, MD, USA, in 2010. Her current research interests include III-V-nitrides, information and power efficiency tradeoffs in mixed-signal integrated circuit design, CMOS biosensors, and CMOS/MEMS integration for lab-on-a-chip technologies. She is currently the TCE Advance Professor

and an Associate Professor with the University of Tennessee, Knoxville, TN, USA, where she is involved in developing smaller and more efficient circuits and devices for sensing systems. Her research group uses mixed signal VLSI to work on integrated smart sensors, hardware security and encryption, and device nanofabrication for applications in biological portable, wearable, and implantable sensing, environmental monitoring, and nuclear science.



Mohammad Aminul Haque (Graduate Student Member, IEEE) received the B.S. degree in applied physics, electronics and communications engineering from the University of Dhaka, Dhaka, Bangladesh, in 2014 and the M.S. degree in electrical engineering from the University of Arkansas, Fayetteville, AR, USA, in 2017. He is currently working toward the Ph.D. degree, under supervision of Dr. Nicole Mc-Farlane. His research interests include semiconductor device fabrication and analog and mixed-signal integrated circuit design. He is currently working on

fabrication and characterization of floating gate circuits for noise optimization in photodetector circuits.